

www.acsami.org Research Article

Probing High-Temperature Oxidation of Thermoelectric Phases $Yb_{14}MSb_{11}$ (M = Mg, Mn, Zn)

Andrew P. Justl and Susan M. Kauzlarich*



Cite This: ACS Appl. Mater. Interfaces 2022, 14, 47246-47254



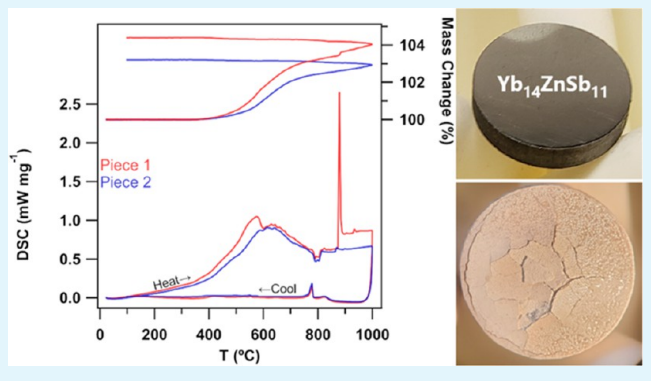
ACCESS

III Metrics & More

Article Recommendations

s Supporting Information

ABSTRACT: $Yb_{14}MSb_{11}$ (M=Mg, Mn, Zn) are p-type Zintl phases with high thermoelectric efficiencies at 1000 °C and melting points above 1200 °C under vacuum and/or inert atmosphere. In a thermoelectric generator, even within a vacuum jacket, small amounts of oxygen may be present, and therefore, elucidating chemical reactions in the presence of air or oxygen provides a framework for engineering design. The oxidation of $Yb_{14}MSb_{11}$ was investigated from room temperature to 1000 °C in dry air with thermogravimetric/differential scanning calorimetry (TG/DSC) on small pellets and visually after heat treatment to 1000 °C under ambient conditions on large pellets. Scanning electron microscopy/energy-dispersive spectroscopy (SEM/EDS) and powder X-ray diffraction provide identification of the oxidation products. In the



presence of dry air, $Yb_{14}MSb_{11}$ initially oxidizes initially slowly at room temperature with a sweeping exotherm and weight gain with rapid oxidation at 400 °C, after which the exotherm signal plateaus at about 600 °C, with M = Zn showing the smallest overall exothermic curve. All samples showed a paired endo-/exotherm at 785-803 °C, consistent with the melting/solidification of $YbSb_{2}$, which in the case of M = Mg, Mn extrudes from the sample. The various sections of the pellets—outer layer, inner layer, and core are analyzed, and oxidation reactions are proposed. After cycling to 1000 °C, the outer layer is composed of Yb_2O_3 with small amounts of the corresponding metal oxides. The inner layer shows delamination by inward diffusion of oxygen and outward diffusion of Sb or Sb oxide-containing phases, and the core shows $Yb_{14}MSb_{11}$. $Yb_{14}ZnSb_{11}$ shows the best resistance to oxidation and may provide a promising material for further passivation optimization.

KEYWORDS: thermoelectrics, space, RTG, oxidation, passivation, Zintl, antimonides

■ INTRODUCTION

Many materials for a variety of energy applications are susceptible to rapid oxidation under potential operating conditions.^{1–7} While excellent properties of a material might be exhibited under an inert atmosphere or vacuum, in the presence of even small amounts of water, oxygen, and heat, these beneficial properties may degrade. In the example of thermoelectric materials, new materials have been prepared, showing high thermoelectric efficiencies, but in many cases, little is known about their oxidation kinetics and chemical reactions at device working temperatures.^{8–12}

Thermoelectric generators utilize the Seebeck effect in a series of p- and n-type materials to produce a usable electric current from a thermal gradient. The heat source producing this thermal gradient can vary from a heat sink rejecting waste heat from an industrial process to heat produced from the decay of a radioisotope in the case of radioisotope thermoelectric generators (RTG). Because these generators contain no moving parts, require little to no maintenance, and are capable of reclaiming energy that would otherwise be rejected as waste heat, they are attractive for

applications such as reclaiming waste heat from combustion engines and deep space exploration.

The materials used within thermoelectric generators are typically doped semiconductors, many of which are prone to oxidation at elevated temperatures. Oxidation of the thermoelectric materials lowers the performance of the device and is one potential failure point of an otherwise robust system. To avoid this, many thermoelectric generator designs utilize an inert atmosphere if operating above the temperature at which the thermoelectric materials oxidize in air. However, it is difficult to remove all oxygen and moisture from the system, so it is important to understand the oxidation process of thermoelectric materials being considered for such a system.

Received: July 21, 2022 Accepted: September 26, 2022 Published: October 11, 2022





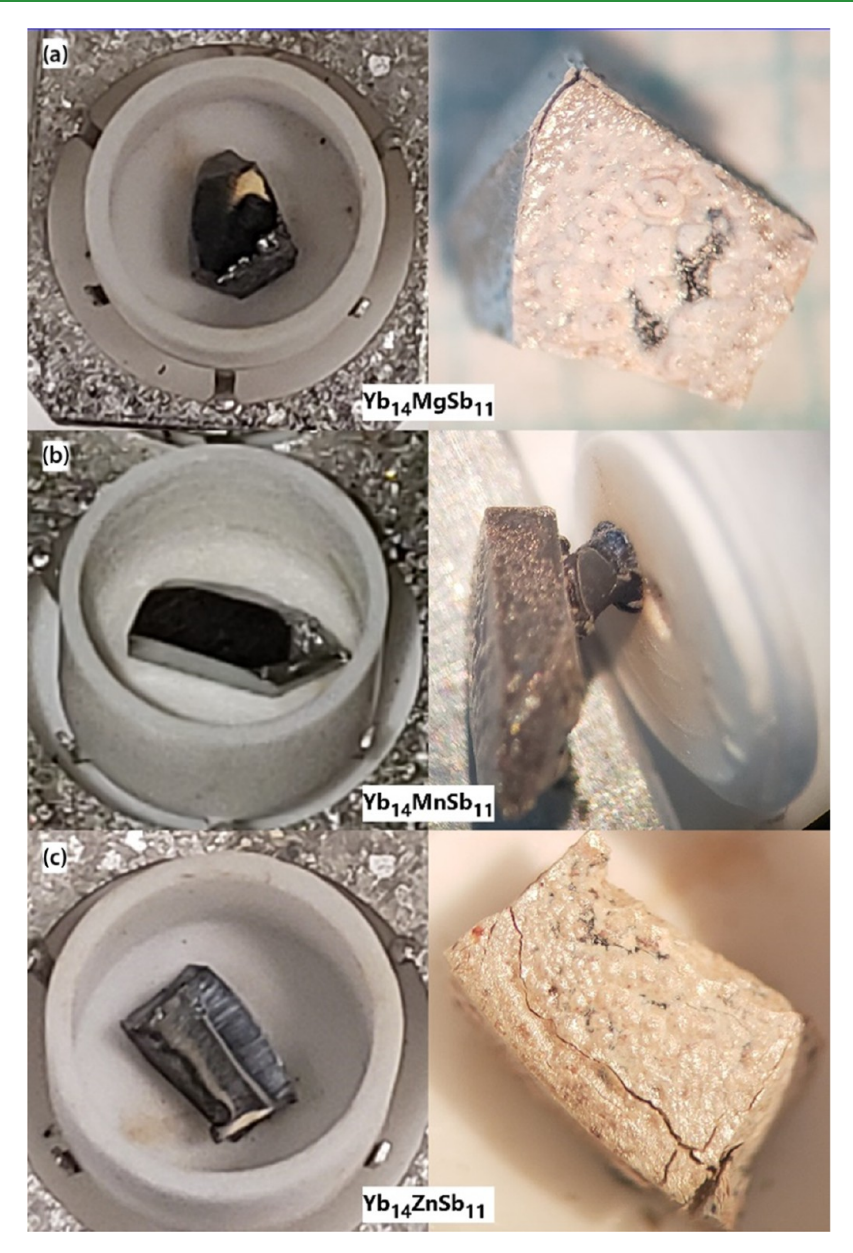


Figure 1. Photographs of samples of Yb₁₄MgSb₁₁ (a), Yb₁₄MnSb₁₁ (b), and Yb₁₄ZnSb₁₁ (c) before (left) and after (right) heating at 10 °C/min under a 50 mL/min flow of dry air from room temperature to 1000 $^{\circ}$ C.

Recent interest in high-temperature power applications and thermoelectric generator design has led to an interest in determining the oxidation behavior of a number of important thermoelectric materials, such as Skutterudites, half Heuslers, and SnSe. 16-21 While Zintl phases show great promise for thermoelectrics, there are few investigations of their stability in air, especially at the proposed operating temperatures. 9,22-25

Yb14MnSb11, along with its structural analogues, Yb₁₄MgSb₁₁, and Yb₁₄ZnSb₁₁, are high-performing p-type thermoelectric materials at high temperatures (>1000 K).²⁶⁻³¹ These phases are under consideration for implementation into the next generation of RTG to power deep space missions. Recent efforts developed a synthetic route to make all three of these thermoelectric materials in high purity through balanced reactions employing binary phases of YbH₂, Yb₄Sb₃, and either Mg₃Sb₂, MnSb, or ZnSb.^{27,32} Hightemperature inert atmosphere measurements show that these phases are stable up to very high temperatures (>1000

 $^{\circ}$ C). $^{9,28,33-35}$ The high-temperature oxidation of Yb₁₄MSb₁₁ (M = Mg, Mn, Zn) made by binary phases is investigated through a combination of thermogravimetry and differential scanning calorimetry (TG/DSC), scanning electron microscopy (SEM) paired with energy-dispersive spectroscopy (EDS), and powder X-ray diffraction (PXRD).

■ EXPERIMENTAL SECTION

Synthesis. Samples of $Yb_{14}MSb_{11}$ (M = Mg, Mn, Zn) were prepared from YbH₂, Yb₄Sb₃, and either Mg₃Sb₂, MnSb, or ZnSb directly via spark plasma sintering, as previously described.²⁷ Powder X-ray diffraction patterns and Rietveld refinement parameters of the samples can be found in the Supporting Information (SI) Figures S1-3 and Table S1.

Thermogravimetry and Differential Scanning Calorimetry (TG/DSC). Oxidation studies of $Yb_{14}MSb_{11}$ (M = Mg, Mn, Zn) were performed using TG/DSC (STA 449 F3 Jupiter, Netzsch) from room temperature to 1000 °C with a heating rate of 10 °C/min under a 50 mL/min flow of dry air (20% O₂, 80% N₂, Praxair) and a 20 mL/min

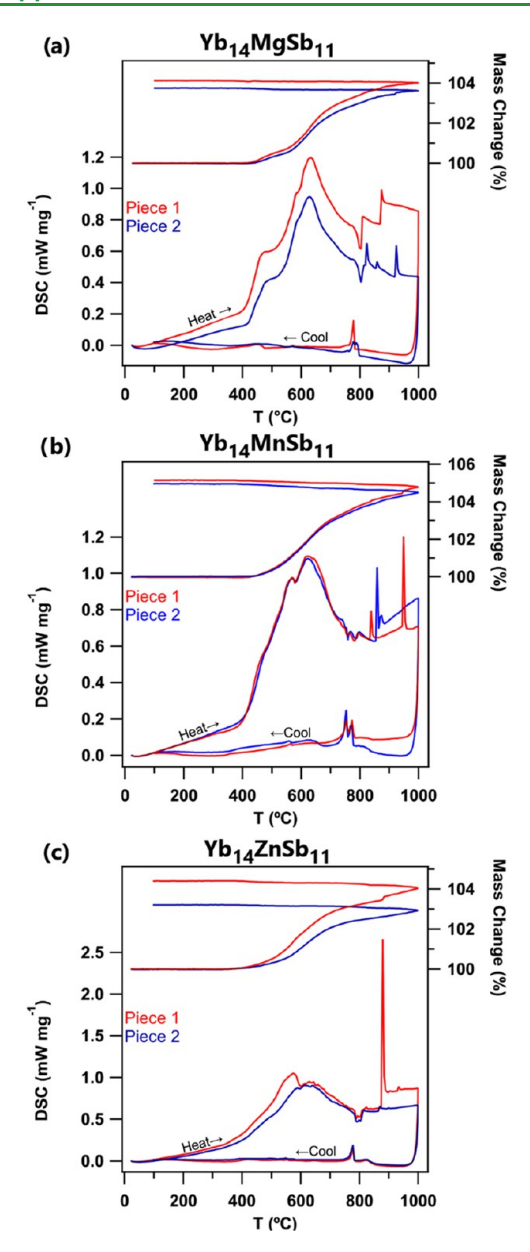


Figure 2. Thermogravimetry (TG) and differential scanning calorimetry (DSC) from room temperature to 1000 °C at a rate of 10 °C/min and under 50 mL/min dry air of the oxidation of two pieces of sample from the pellets of Yb₁₄MgSb₁₁ (a), Yb₁₄MnSb₁₁ (b), and Yb14ZnSb11 (c). Two separate experiments are shown on each plot in different colors (pieces 1 and 2). The DSC curves are shown on the bottom using the left axis, and the TG curves are plotted on the top using the right.

protective flow of Ar (99.999%, Praxair). The studies were done using alumina crucibles, which were heat treated by a 30-minute anneal under Ar flow at 1100 °C in the instrument prior to performing the experiment. Two separate pieces of each $Yb_{14}MSb_{11}$ (M = Mg, Mn, Zn) pellet were run in the oxidation studies to check the reproducibility of data. After oxidation, one piece was ground for PXRD, and the other was set in epoxy and polished for SEM/ EDS.

Pellet Oxidation Studies. Disk-shaped pellets (12.7 mm dia., ~3 mm thick) of $Yb_{14}MSb_{11}$ (M = Mg, Mn, Zn) were polished using progressively finer sandpaper (400 to 1200 grit) to achieve a parallel, mirrored surface. They were then placed in an alumina assembly which held the pellet at three points but minimized the contact between the alumina and Yb₁₄MSb₁₁ pellet. The assembly and pellet were then placed in a box furnace with a fire brick set to reduce the

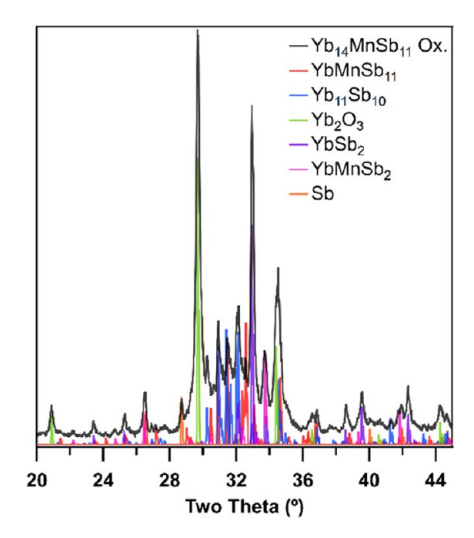


Figure 3. Powder X-ray diffraction pattern of Yb14MnSb11 after oxidation to 1000 °C in the TG/DSC experiment described above.

internal volume and bring the sample closer to the thermocouple. It was then set to heat to 1000 °C at a rate of 200 °C/h and dwell there for 12 h. The oxidized pellets were then broken in half: half was set in epoxy for electron microscopy, and half was dissected using tweezers and a razor to perform powder X-ray diffraction on the different components.

Powder X-ray Diffraction. Powder X-ray diffraction (PXRD) was performed on slices of the $Yb_{14}MSb_{11}$ (M = Mg, Mn, Zn) pellets before oxidation and on samples after oxidation. Studies were done on a Bruker D8 Advanced Eco using Cu K α radiation with a Ni K $_{\beta}$ filter and a zero background SiO₂ plate. PXRD patterns were then analyzed using the JANA2006 software package.3

Electron Microscopy and Elemental Mapping. Samples were set in epoxy and sanded with a progressively finer abrasive to reveal the cross sections. Samples were coated with a thin film of carbon using a Quorum Tech Q150RES sputterer and carbon cord evaporation system. Scanning electron microscopy (SEM) was performed using a Thermo Fisher Quattro environmental scanning electron microscope on carbon-coated samples set in epoxy. Energydispersive spectroscopy (EDS) was also performed using the same instrument equipped with a Bruker XFlash 6130 detector. Bruker Quantax software was used for analysis, and single crystals of Yb₁₄MnSb₁₁, Yb₁₄MgSb₁₁, and a piece of Zn metal (99.9999%, Johnson Matthey) were used as standards.

RESULTS AND DISCUSSION

Thermogravimetry and Differential Scanning Calorimetry Studies. Figure 1 shows the photos (before and after heating) of pieces of Yb14MnSb11, Yb14MgSb11, and Yb₁₄ZnSb₁₁ in TG/DSC alumina crucibles oxidized by heating in a dry air atmosphere from room temperature to 1000 °C. Before oxidation, all three analogues appear as highly polished, reflective, black materials. Upon cycling the samples to 1000 °C under air, there was a distinct change in the appearance of the samples. The sample of Yb₁₄MgSb₁₁ (Figure 1a) developed a glossy, white outer layer. Along with the formation of an outer layer around the sample, there appeared to be a small amount of black material melting out of the oxidized sample. In contrast to the Mg analogue, the Yb₁₄MnSb₁₁ (Figure 1b) developed a glossy brownish-black outer layer on the exterior of the sample. Much like the Yb14MgSb11 sample, there was also black material that appeared to extrude from the sample. When Mg or Mn was exchanged for Zn in Yb₁₄ZnSb₁₁ (Figure 1c), the sample developed a glossy white outer layer much like

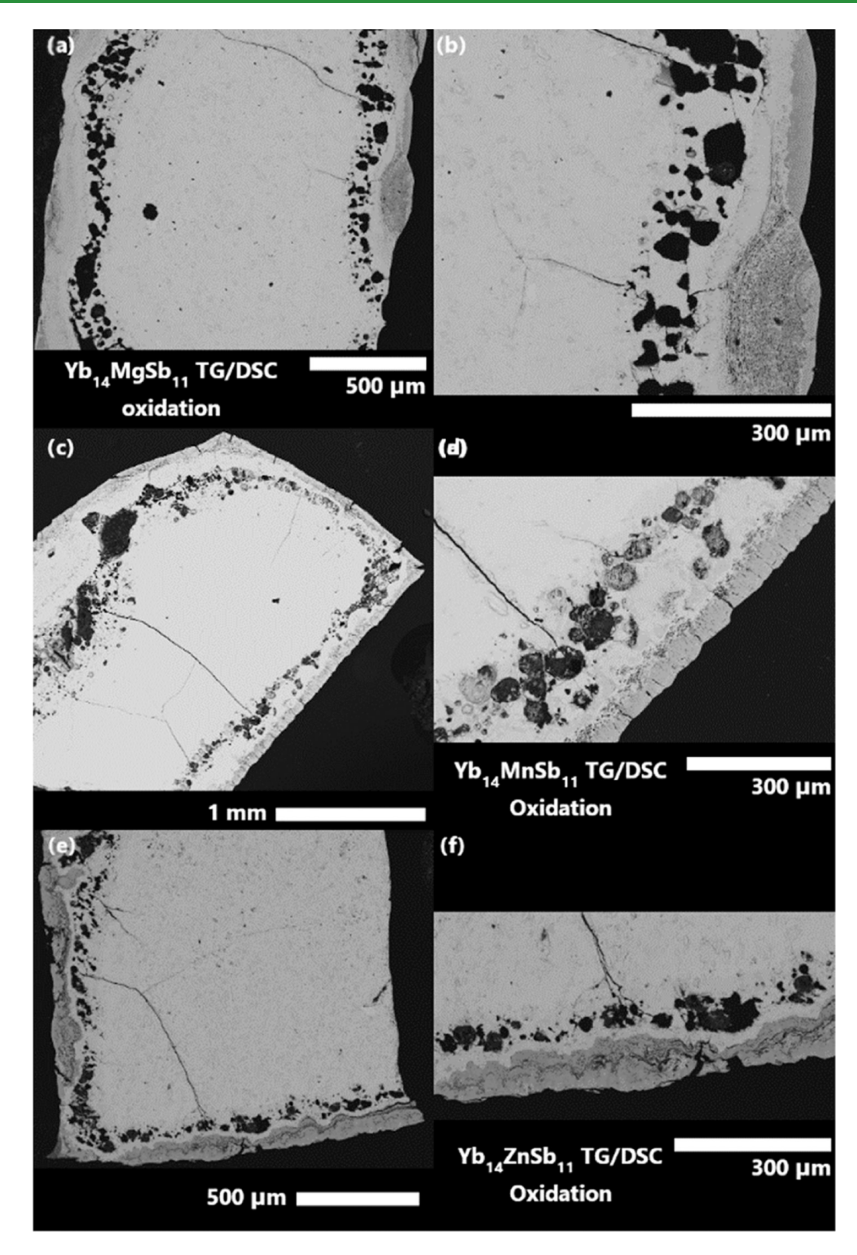


Figure 4. Backscattered electron micrographs of $Yb_{14}MgSb_{11}$ (a) and (b), $Yb_{14}MnSb_{11}$ (c) and (d), and $Yb_{14}ZnSb_{11}$ (e) and (f) after air oxidation in the TG/DSC.

 $Yb_{14}MgSb_{11}$ with a minimal amount of black material, which extruded from the underside of the sample. In these studies, there was a minimal reaction between the samples and the Al_2O_3 crucible. However, there was a significant reaction of the extruded material with the crucible. This is most evident for $Yb_{14}MnSb_{11}$, where the extruded material attached to the lid of the crucible, as shown in (Figure 1b).

Figure 2 provides the TG/DSC curves for the oxidation of the samples shown in Figure 1 from room temperature to 1000 $^{\circ}$ C, along with a second piece of the same sample pellet, $Yb_{14}MSb_{11}$ (M = Mg, Mg, Mg, Mg, to check reproducibility. On heating, the DSC signal begins a sweeping exotherm at 200 $^{\circ}$ C, which increases in slope at 400 $^{\circ}$ C. This correlates with the increase in mass gain seen in the TG signal and can be attributed to the oxidation processes occurring at the surface of the $Yb_{14}MSb_{11}$ (M = Mn, Mg, Zn) sample. At temperatures above 615 $^{\circ}$ C, the sweeping exotherm decreases in magnitude. Between 785–803 $^{\circ}$ C in the heating portion of the cycles,

there is a sharp endotherm with a corresponding exotherm in the cooling cycle. This event likely corresponds to the melting and solidification of the material seen extruding from the sample. In the case of Yb₁₄MnSb₁₁, there is an additional set of endo- and exotherms around 755 °C after this event, which suggests that there may be an additional melting point or eutectic within the melted material in this system. At about 900 °C, most of the DSC curves showed one sharp exotherm with no corresponding endotherm on cooling. This event likely corresponds to the reaction between the melted material and the Al₂O₃ crucible after the melt broke through the outer oxidation layer of the piece. This hypothesis is supported by the fact that the temperature of this exotherm appears to change for each piece, even for the same sample pellet, suggesting that a rupture happens at slightly different temperatures. This exotherm does not appear in the DSC curve for piece 2 of Yb₁₄ZnSb₁₁, which also did not show melted/extruded material. The TG for all samples showed a

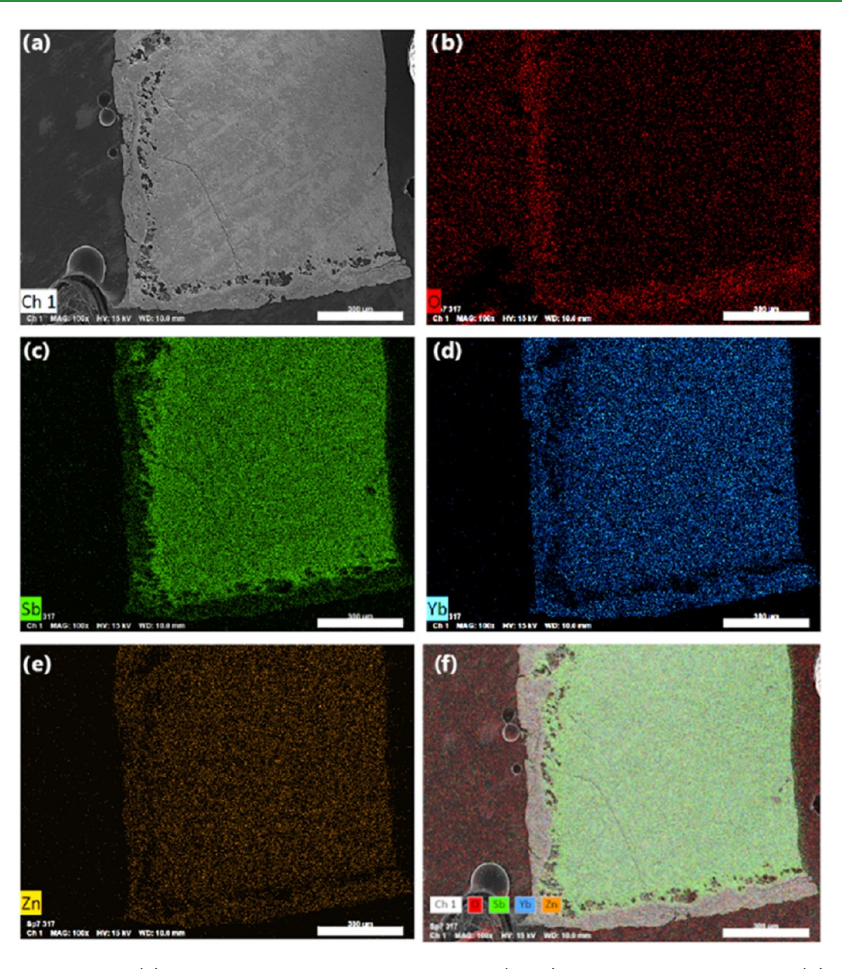


Figure 5. Secondary electron micrograph (a) and energy-dispersive spectroscopy (EDS) elemental mapping of O (b), Sb (c), Yb (d), Zn (e), and combined (f) for a sample of $Yb_{14}ZnSb_{11}$ after air oxidation to 1000 °C. Scale bars are all 300 μ m.

consistent mass gain (4-5%) on heating, but on cooling, the samples showed a relatively steady mass, which suggests that the surface oxidation of the $Yb_{14}MSb_{11}$ (M = Mn, Mg, Zn) sample may passivate the internal material from further oxidation. This agrees well with the parabolic kinetics seen in the isothermal oxidation of $Yb_{14-x}RE_xMnSb_{11}$ (RE = La – Lu, except for Ce and Eu) single crystals.³⁴ The TG/DSC of the oxidation of both pieces of each Yb14MSb11 pellet agree well with each other in the onset of oxidation along with the observed onset of endo- and exotherms in the moderate temperature range. There is a wide degree of variation in the onset of the high-temperature nonreversible exotherm due to differences in when the molten material broke through the outer layer and contacted the Al₂O₃ crucible. An overlay of the DSC from the oxidation of all three analogues can be found in the SI, Figure S4 for comparison.

Powder X-ray diffraction on these samples after oxidation (Figure 3 and SI Figures S5 and S6) showed a mixture of Yb₁₄MSb₁₁, Yb₁₁Sb₁₀, YbSb₂, Yb₂O₃, and Sb. In the case of Yb₁₄MnSb₁₁, shown in Figure 3, additional peaks assigned to YbMnSb₂ were identified in the diffraction pattern. Because the oxidized samples consist of the starting Yb₁₄MSb₁₁, more Sb-rich YbSb binary phases such as YbSb₂ and Yb₂O₃, it is possible there is a series of successive oxidation reactions occurring.

Figure 4 shows the backscattered electron micrographs for sections of the oxidized samples of $Yb_{14}MSb_{11}$ (M = Mg, Mn, Zn) from the TG/DSC experiment. All samples show a

continuous crust that is ~100 μ m thick on the surface (outer layer) with a porous region (inner layer) surrounding a solid core. The porosity below the surface (inner layer) suggests material loss, presumably from sublimation, during the oxidation of the sample. By backscattered electrons, the most noticeable difference is between the lighter interior and darker outer crust region, which suggests a significant compositional difference

Energy-dispersive spectroscopy (EDS) and X-ray mapping (Figure 5 and SI Figures S7 and S8) show that oxygen is largely segregated to the outer layer of the sample. The outer layer is also notably void of Sb relative to the rest of the sample. EDS showed atomic concentrations which corresponded to Yb2O3, along with small amounts of Mg, Mn, or Zn, likely in the form of an oxide along with small amounts of Sb. There is a lessened concentration of oxygen along with an increase in the Sb concentration in the porous region. EDS showed this region to have atomic concentrations consistent with YbSb₂ and small amounts of oxide. The interior of the sample (core) showed the lowest concentration of oxygen (~3 atom %) along with the concentration of Yb, M, and Sb, which were close to that of Yb14MSb11. The high oxygen concentrations and low Sb concentrations within the outer layer suggest that once all of the Yb and metal (Mg, Mn, Zn) have gone to their respective oxides, there is elemental Sb, which likely forms Sb₂O₃ and sublimes from the sample at high temperatures. This is likely the formation mechanism of the porous inner layer.

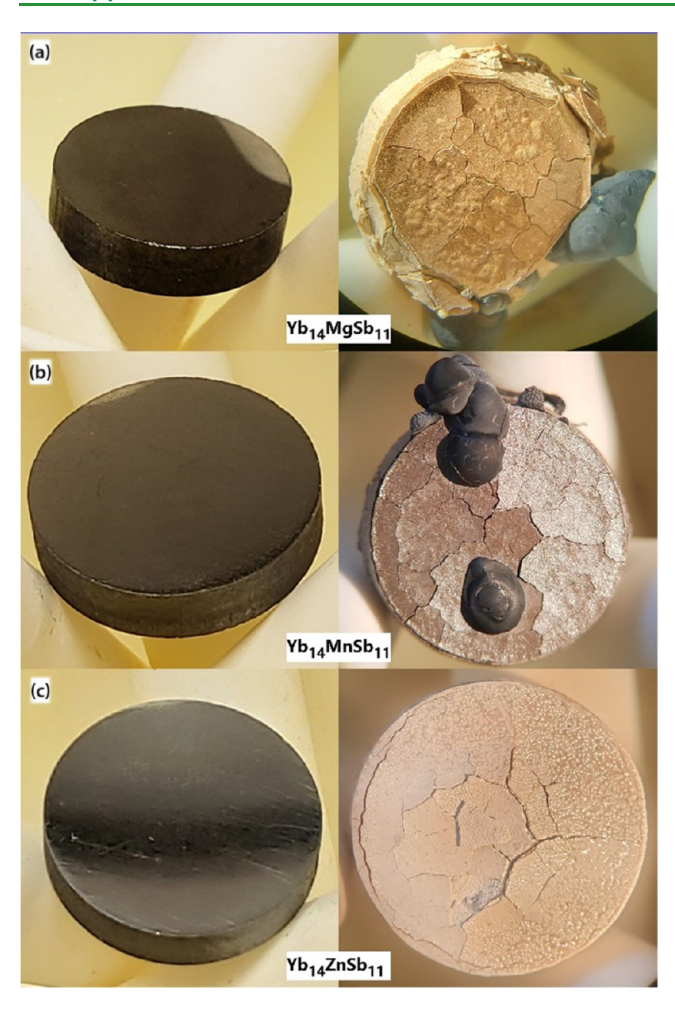


Figure 6. Pellets of $Yb_{14}MgSb_{11}$ (a), $Yb_{14}MnSb_{11}$ (b), and $Yb_{14}ZnSb_{11}$ (c) before (left) and after (right) oxidation under ambient conditions at 1000 °C for 12 h.

Large-Scale Pellet Studies. To compare how these oxide coatings formed on a larger scale under atmospheric conditions (as opposed to controlled dry air), whole pellets (12.7 mm dia. \times ~3 mm thick) were heated in a box furnace under atmospheric conditions from room temperature to 1000 °C at a rate of 200 °C/h and held for 12 h. Figure 6 shows the before (left) and after (right) photos of the oxidized pellets. After 12 h at 1000 °C, the pellet of Yb₁₄MgSb₁₁ developed a glossy offwhite/tan outer layer, which showed heavy cracking and crumbling at the corners. Although not clearly visible in Figure 6, there was also a black material, which appeared to have melted out of the sample, much like what was seen for the samples in the TG/DSC experiments. The Yb14MnSb11 pellet developed a glossy brown-black outer layer, which showed cracking at the corners and across the face of the pellet. Figure 6 clearly shows the black material of the surface that melted out of the sample. The Yb14ZnSb11 developed a glossy white outer layer with less cracking than what was seen for the other two analogues. What is also noticeable is the lack of black material melting out of this sample. However, there is bulging seen on both faces of the pellet, which is likely a result of the expansion of a molten phase that may be not significant enough to break through the outer layer. Additional photos of the oxidized pellets and cross sections can be found in the SI, Figures S9–S11.

Figure 7 shows backscattered electron micrographs of the cross sections of the oxidized large pellets from Figure 6a,b (Yb₁₄MnSb₁₁) and Figure 6c, d (Yb₁₄ZnSb₁₁). The cross sections of portions of the large Yb14MgSb11 pellet can be found in the SI, Figure S12. In both Yb14MnSb11 and Yb₁₄ZnSb₁₁, there are similar results to what was seen in the cross sections of TG/DSC-oxidized samples. The outside of both samples is surrounded by a darker outer layer that extends \sim 150–200 μ m below the surface. Some regions of this outer layer show cracking. Inside of that is a small gap and porous region. Notably, the gap between the core and outer layer in the Yb14MnSb11 sample is larger than that seen in the sample of Yb₁₄ZnSb₁₁. In the center of each sample is a solid core. In the case of Yb₁₄MnSb₁₁, the core has taken on a semi-circular shape, which is quite different from the Yb14ZnSb11, which retained its rectangular cross section. The difference between the size of the gap between the core and outer layer along with the core shape are likely a result of the large amount of material that melted out of the sample of Yb14MnSb11 and can be seen in the bottom left corner of Figure 7a.

PXRD was performed on the individual components of these oxidized samples and can be seen in Figure 8 for Yb₁₄MnSb₁₁ and in SI Figure S13 $(Yb_{14}MgSb_{11})$ and S14 $(Yb_{14}ZnSb_{11})$. The black material which extruded from Yb14MgSb11 was found to be a mixture of YbSb₂, Yb₂O₃, and Sb. In the case of Yb₁₄MnSb₁₁, the resulting melt was found to consist of YbSb₂, Yb₂O₃, and Sb, along with the addition of YbMnSb₂. The difference in the composition of the melt agrees with the single exotherm and corresponding endotherm seen in the DSC on cycling Yb14MgSb11 in dry air as compared to the two coupled exo- and endotherms seen in the DSC of Yb₁₄MnSb₁₁. There was no extrusion or melt from the large Yb₁₄ZnSb₁₁ pellet. The oxidized Yb₁₄MnSb₁₁ sample's outer layer was found to consist of YbMnSb₂ in addition to Yb₂O₃, YbSb₂, and Sb. The outer light brown layers of the large pellets of Yb14MgSb11 and Yb₁₄ZnSb₁₁ were found to be made of Yb₂O₃, Yb₃O₄, YbSb₂, and Sb. The core of the Yb14MnSb11 shows the addition of YbMnSb₂ in addition to the Yb₂O₃, YbSb₂, Sb, Yb₁₁Sb₁₀, and Yb₁₄MnSb₁₁. The presence of small amounts of YbSb₂, YbMnSb₂, and Sb is likely a result of the porous region remaining attached to the surface of the core material. The solid inner cores of Yb₁₄MgSb₁₁ and Yb₁₄ZnSb₁₁ were found to consist of small amounts of Yb₂O₃, YbSb₂, and Sb, along with Yb₁₁Sb₁₀ and Yb₁₄MgSb₁₁ or Yb₁₄ZnSb₁₁. Because the outer layer consisted of YbSb₂, Sb, and Yb₂O₃ and the inner part of the sample contained more Yb-rich phases such as Yb₁₁Sb₁₀, and Yb14MSb11, it is likely that oxidation occurs along a successive pathway.

Equations 1–6 provide a possible pathway for the successive oxidation of $Yb_{14}ZnSb_{11}$, the simplest system to analyze. In this reaction scheme, the $Yb_{14}ZnSb_{11}$ initially $(200-600\ ^{\circ}C)$ oxidizes to Yb_2O_3 , ZnO, and $Yb_{11}Sb_{10}$. The $Yb_{11}Sb_{10}$ could go on to form Yb_2O_3 and YbSb (eq 2), the Sb-rich adjacent phase to $Yb_{11}Sb_{10}$, but because it was not observed in the PXRD and is predicted to be metastable, it is more likely that $Yb_{11}Sb_{10}$ forms Yb_2O_3 and $YbSb_2$ upon oxidation instead (eq 3) at $785-803\ ^{\circ}C$. According to the phase diagram, $YbSb_2$ melts incongruently at $805\ ^{\circ}C$, consistent with couple endoand exotherm. 38 In the case of $Yb_{14}MnSb_{11}$, the $YbMnSb_2$ product observed by PXRD is likely a result of the solubility of Mn within the Sb-rich $YbSb_2$ phase, especially once it is molten.

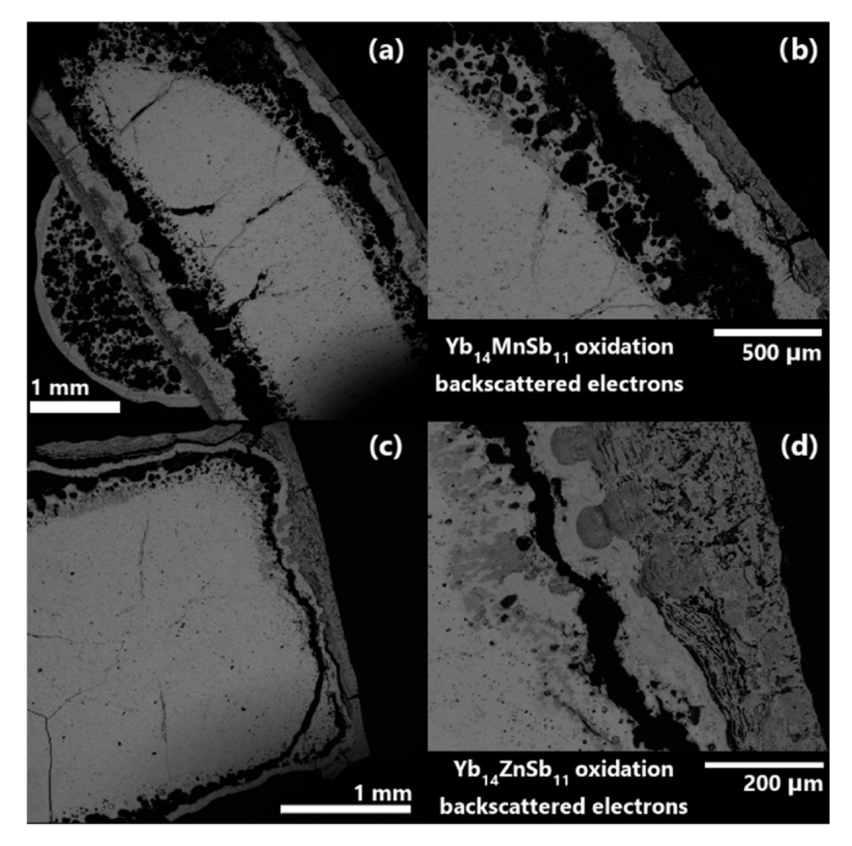


Figure 7. Backscattered electron micrographs of the cross sections of large pellets of Yb₁₄MnSb₁₁ (a, b) and Yb₁₄ZnSb₁₁ (c, d) after oxidation under ambient conditions to 1000 °C.

$$Yb_{14}ZnSb_{11} + O_2 \rightarrow Yb_2O_3 + ZnO + Yb_{11}Sb_{10}$$
 (1)

$$Yb_{11}Sb_{10} + O_2 \rightarrow Yb_2O_3 + YbSb$$
 (2)

$$Yb_{11}Sb_{10} + O_2 \rightarrow Yb_2O_3 + YbSb_2$$
 (3)

$$YbSb + O_2 \rightarrow Yb_2O_3 + YbSb_2 \tag{4}$$

$$YbSb_2 + O_2 \rightarrow Yb_2O_3 + Sb \tag{5}$$

$$Sb + O_2 \rightarrow Sb_2O_3 \rightarrow Sb_4O_{6(g)}$$
(6)

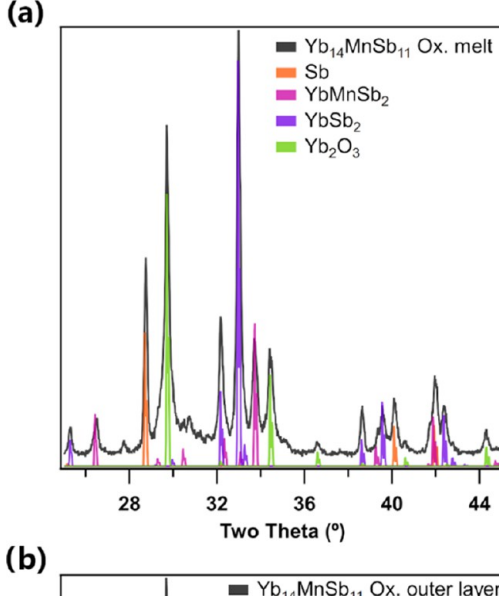
Equations 1–6. Possible reactions for the successive oxidation of $Yb_{14}ZnSb_{11}$.

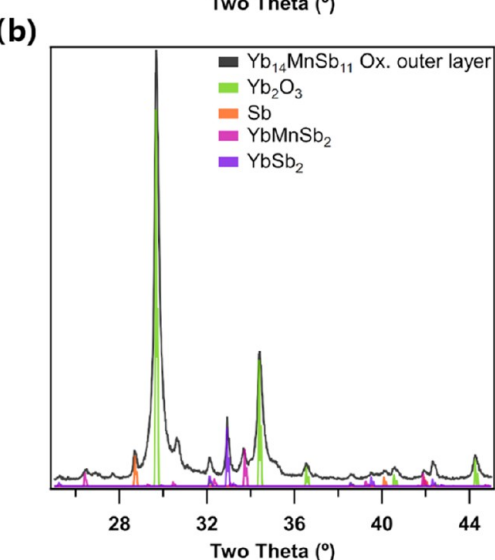
This reaction pathway would explain the presence of the respective phases within the different regions of the samples. The outer layer forming at low temperatures (200–600 $^{\circ}$ C) from the reaction (eqs 1, 3, and 5) would explain the glossy appearance and robustness of the outer layer as the Sb would act as a flux for the Yb₂O₃ forming at high temperatures. The Sb would then oxidize (eq 6) and successively sublimate, leaving the outer layer relatively void of Sb, as seen in the EDS. Because the oxidation appears as a sweeping exotherm in the DSC, it is likely that once (eq 1) is initiated, the reactions (eqs 2–4) occur concurrently with the final oxidation reactions of (eqs 5 and 6) as oxygen diffuses more rapidly into the system with temperature.

CONCLUSIONS

Through both small-scale TG/DSC experiments and largerscale oxidation experiments on whole pellets of Yb₁₄MgSb₁₁, Yb₁₄MnSb₁₁, and Yb₁₄ZnSb₁₁ it was found that all three analogues oxidized through a similar pathway. These reactions resulted in the decomposition of Yb₁₄MSb₁₁ to form Yb₂O₃, M_xO_v , $Yb_{11}Sb_{10}$, $YbSb_2$, and Sb. In the case of $Yb_{14}MnSb_{11}$, there was also the addition of YbMnSb₂. PXRD and SEM/EDS experiments revealed that the outer layer of the oxidized samples consisted of Yb₂O₃, along with YbSb₂, Sb, and small amounts of metal (Mg, Mn, or Zn) oxide. Interior to that was a porous region (inner layer) found to consist mostly of YbSb₂, along with YbMnSb₂ in the case of Yb₁₄MnSb₁₁. The core of the sample was found to consist of Yb₁₄MSb₁₁ and Yb₁₁Sb₁₀, along with small amounts of Yb2O3, YbSb2, and Sb. These results suggest that the oxidation of Yb14MgSb11, Yb14MnSb11, and Yb14ZnSb11 progress through a similar succession of oxidation reactions, initially forming Yb11Sb10, Yb2O3, and metal oxide (Mg, Mn, or Zn). $Yb_{11}Sb_{10}$ further oxidizes to YbSb₂ and Yb₂O₃ and finally to Yb₂O₃ and Sb. Under air oxidation and higher temperatures, Sb goes on to form Sb₂O₃, which then forms Sb₄O₆ and sublimes away from the surface of the sample. While the oxidation of these samples creates a chemically bonded glossy oxide outer layer, the formation and successive melting of YbSb₂ in these heavily oxidized samples proved problematic. The sample showing the least impact of YbSb₂ was Yb₁₄ZnSb₁₁, which might be attributed to the smaller unit cell of Yb₁₄ZnSb₁₁, which would result in shorter, stronger bonds and slower oxidation kinetics.

These results suggest that if these materials were oxidized at lower temperatures or in lower concentration oxygen environments, it may be possible to use oxidation to create effective sublimation barriers for use in inert atmospheres. The oxidation pathway of $Yb_{14}MSb_{11}$ (M=Mg,Mn,Zn) is markedly unique in comparison to many other Sb-containing binary and ternary systems, which typically form M-Sb-O ternary phases. These results may be applicable to the





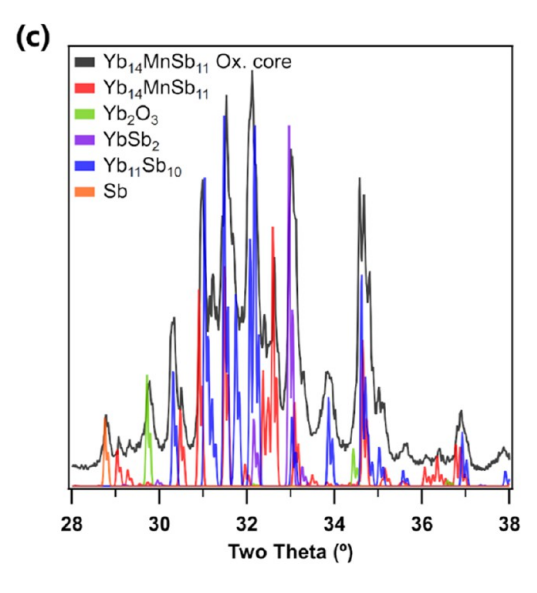


Figure 8. PXRD of the melt (a), outer layer (b), and core sections (c) of the large Yb14MnSb11 pellet oxidized under ambient conditions to 1000 °C. Experimental patterns are shown in black, while simulated patterns for phases present are shown in colors.

oxidation of other complex intermetallic systems and a possible route to forming passivation barriers in these systems.

ASSOCIATED CONTENT

Supporting Information

The Supporting Information is available free of charge at https://pubs.acs.org/doi/10.1021/acsami.2c13093.

> PXRD and Rietveld refinement parameters of Yb₁₄MSb₁₁ (M = Mg, Mn, Zn) samples; DSC curves of the oxidation of $Yb_{14}MSb_{11}$ (M = Mg, Mn, Zn) overlayed for comparison; PXRD of Yb₁₄MgSb₁₁ and Yb₁₄ZnSb₁₁ after oxidation in the TG/DSC; EDS elemental mapping of the TG/DSC-oxidized samples; additional pictures of the oxidized $Yb_{14}MSb_{11}$ (M = Mg, Mn, Zn) pellets; backscattered SEM micrographs of portions of the oxidized Yb14MgSb11; and PXRD of the different components of the oxidized Yb14MgSb11 and Yb₁₄ZnSb₁₁ pellets (PDF)

AUTHOR INFORMATION

Corresponding Author

Susan M. Kauzlarich - Department of Chemistry, University of California, Davis, California 95616, United States;

orcid.org/0000-0002-3627-237X; Email: smkauzlarich@ucdavis.edu

Author

Andrew P. Justl – Department of Chemistry, University of California, Davis, California 95616, United States; orcid.org/0000-0001-6332-4545

Complete contact information is available at: https://pubs.acs.org/10.1021/acsami.2c13093

Notes

The authors declare no competing financial interest.

ACKNOWLEDGMENTS

This work was supported by NSF DMR-2001156. This research used the Advanced Materials Characterization and Testing laboratory (AMCaT) at the University of California, Davis, for SEM/EDS data which is supported by NSF DMR-1725618. SEM samples were carbon-coated in the Center for Nano-MicroManufacturing (CNM2) at UC Davis. The authors thank Drs Sabah Bux, Dean Cheikh, and Max Wood for useful discussion.

REFERENCES

- (1) Rinkel, B. L. D.; Hall, D. S.; Temprano, I.; Grey, C. P. Electrolyte Oxidation Pathways in Lithium-Ion Batteries. J. Am. Chem. Soc. 2020, 142, 15058-15074.
- (2) Kang, H. B.; Saparamadu, U.; Nozariasbmarz, A.; Li, W.; Zhu, H.; Poudel, B.; Priya, S. Understanding Oxidation Resistance of Half-Heusler Alloys for in-Air High Temperature Sustainable Thermoelectric Generators. ACS Appl. Mater. Interfaces 2020, 12, 36706-36714.
- (3) Xia, X.; Qiu, P.; Huang, X.; Wan, S.; Qiu, Y.; Li, X.; Chen, L. Oxidation Behavior of Filled Skutterudite CeFe₄Sb₁₂ in Air. J. Electron. Mater. 2014, 43, 1639-1644.
- (4) Drevet, R.; Aranda, L.; Petitjean, C.; David, N.; Veys-Renaux, D.; Berthod, P. Oxidation Behavior of the Skutterudite Material Ce_{0.75}Fe₃CoSb₁₂. Oxid. Met. **2019**, 91, 767–779.

- (5) Kane, K. A.; Pint, B. A.; Mitchell, D.; Haynes, J. A. Oxidation of Ultrahigh Temperature Ceramics: Kinetics, Mechanisms, and Applications. J. Eur. Ceram. Soc. 2021, 41, 6130-6150.
- (6) Hou, F.; Zhang, D.; Sharma, P.; Singh, S.; Wu, T.; Seidel, J. Oxidation Kinetics of WTe2 Surfaces in Different Environments. ACS Appl. Electron. Mater. 2020, 2, 2196-2202.
- (7) Leszczynski, J.; Wojciechowski, K. T.; Malecki, A. L. Studies on Thermal Decomposition and Oxidation of CoSb₃. J. Therm. Anal. Calorim. 2011, 105, 211-222.
- (8) Gucci, F.; D'Isanto, F.; Zhang, R.; Reece, M.; Smeacetto, F.; Salvo, M. Oxidation Protective Hybrid Coating for Thermoelectric Materials. Materials 2019, 12, 573.
- (9) Nesbitt, J. A.; Opila, E. J.; Nathal, M. V. In Situ Growth of a Yb2O3 Layer for Sublimation Suppression for Yb14MnSb11 Thermoelectric Material for Space Power Applications. J. Electron. Mater. 2012, 41, 1267-1273.
- (10) Dong, H.; Li, X.; Huang, X.; Zhou, Y.; Jiang, W.; Chen, L. Improved Oxidation Resistance of Thermoelectric Skutterudites Coated with Composite Glass. Ceram. Int. 2013, 39, 4551-4557.
- (11) Skomedal, G.; Kristiansen, N. R.; Sottong, R.; Middleton, H. Evaluation of Thermoelectric Performance and Durability of Functionalized Skutterudite Legs. J. Electron. Mater. 2017, 46, 2438-2450.
- (12) Shi, X.-L.; Zou, J.; Chen, Z.-G. Advanced Thermoelectric Design: From Materials and Structures to Devices. Chem. Rev. 2020, 120, 7399-7515.
- (13) Beretta, D.; Neophytou, N.; Hodges, J. M.; Kanatzidis, M. G.; Narducci, D.; Martin- Gonzalez, M.; Beekman, M.; Balke, B.; Cerretti, G.; Tremel, W.; et al. Thermoelectrics: From History, a Window to the Future. Mater. Sci. Eng., R 2019, 138, No. 100501.
- (14) Yan, Q.; Kanatzidis, M. G. High-Performance Thermoelectrics and Challenges for Practical Devices. Nat. Mater. 2022, 21, 503-513.
- (15) LeBlanc, S. Thermoelectric Generators: Linking Material Properties and Systems Engineering for Waste Heat Recovery Applications. Sustainable Mater. Technol. 2014, 1-2, 26-35.
- (16) Zhao, D.; Tian, C.; Tang, S.; Liu, Y.; Chen, L. High Temperature Oxidation Behavior of Cobalt Triantimonide Thermoelectric Material. J. Alloys Compd. 2010, 504, 552-558.
- (17) Kang, H. B.; Saparamadu, U.; Nozariasbmarz, A.; Li, W.; Zhu, H.; Poudel, B.; Priya, S. Understanding Oxidation Resistance of Half-Heusler Alloys for in-Air High Temperature Sustainable Thermoelectric Generators. ACS Appl. Mater. Interfaces 2020, 12, 36706-
- (18) Hara, R.; Inoue, S.; Kaibe, H. T.; Sano, S. Aging Effects of Large-Size n-Type CoSb₃ Prepared by Spark Plasma Sintering. J. Alloys Compd. 2003, 349, 297-301.
- (19) Berche, A.; Jund, P. Oxidation of Half-Heusler NiTiSn Materials: Implications for Thermoelectric Applications. Intermetallics
- (20) Drevet, R.; Aranda, L.; David, N.; Benyahia, M.; Kenfaui, D.; Masschelein, P.; Candolfi, C.; Lenoir, B.; Monnier, J.; Dauscher, A.; et al. Oxidation Behavior of the Skutterudite Material Yb0.2Co4Sb12. Metall. Mater. Trans. A 2021, 52, 3996-4002.
- (21) Li, Y.; He, B.; Heremans, J. P.; Zhao, J. C. High-Temperature Oxidation Behavior of Thermoelectric SnSe. J. Alloys Compd. 2016, 669, 224-231.
- (22) Kauzlarich, S. M.; Zevalkink, A.; Toberer, E.; Snyder, G. J.Chapter 1. Zintl Phases: Recent Developments in Thermoelectrics and Future Outlook. In Thermoelectric Materials and Devices; Nandhakumar, I.; White, N. M.; Beeby, S., Eds.; Royal Society of Chemistry, 2016; Vol. 2017, pp 1-26 DOI: 10.1039/ 9781782624042-00001.
- (23) Kauzlarich, S. M.; Devlin, K. P.; Perez, C. J.Zintl Phases for Thermoelectric Applications. In Thermoelectric Energy Conversion; Funahashi, R., Ed.; Woodhead Publishing, 2021; pp 157-182 DOI: 10.1016/b978-0-12-818535-3.00004-9.
- (24) Condron, C. L.; Kauzlarich, S. M.; Gascoin, F.; Snyder, G. J. Thermoelectric Properties and Microstructure of Mg₃Sb₂. J. Solid State Chem. 2006, 179, 2252-2257.

- (25) Paik, J. A.; Caillat, T.Alumina Paste Layer As A Sublimation Suppression Barrier For Yb₁₄MnSb₁₁; NASA Tech Briefs, 2010; pp 22-
- (26) Brown, S. R.; Kauzlarich, S. M.; Gascoin, F.; Snyder, G. J. Yb₁₄MnSb₁₁: New High Efficiency Thermoelectric Material for Power Generation. Chem. Mater. 2006, 18, 1873-1877.
- (27) Justl, A. P.; Cerretti, G.; Bux, S. K.; Kauzlarich, S. M. 2 + 2 = 3: Making Ternary Phases through a Binary Approach. Chem. Mater. 2022, 34, 1342-1355.
- (28) Grebenkemper, J. H.; Hu, Y.; Barrett, D.; Gogna, P.; Huang, C.-K.; Bux, S. K.; Kauzlarich, S. M. High Temperature Thermoelectric Properties of Yb₁₄MnSb₁₁ Prepared from Reaction of MnSb with the Elements. Chem. Mater. 2015, 27, 5791-5798.
- (29) Perez, C. J.; Wood, M.; Ricci, F.; Yu, G.; Vo, T.; Bux, S. K.; Hautier, G.; Rignanese, G.-M.; Snyder, G. J.; Kauzlarich, S. M. Discovery of Multivalley Fermi Surface Responsible for the High Thermoelectric Performance in Yb₁₄MnSb₁₁ and Yb₁₄MgSb₁₁. Sci. Adv. 2021, 7, No. eabe9439.
- (30) Hu, Y.; Wang, J.; Kawamura, A.; Kovnir, K.; Kauzlarich, S. M. Yb14MgSb11 and Ca14MgSb11 - New Mg-Containing Zintl Compounds and Their Structures, Bonding, and Thermoelectric Properties. Chem. Mater. 2015, 27, 343-351.
- (31) Justl, A. P.; Cerretti, G.; Bux, S. K.; Kauzlarich, S. M. Hydride Assisted Synthesis of the High Temperature Thermoelectric Phase: Yb₁₄MgSb₁₁. J. Appl. Phys. 2019, 126, No. 165106.
- (32) Justl, A. P.; Ricci, F.; Cerretti, G.; Pike, A.; Bux, S. K.; Hautier, G.; Kauzlaricha, S. M. Unlocking the Thermopower of the Ca₁₄AlSb₁₁ Structure Type. Sci. Adv. 2022, 8, No. eabq3780.
- (33) Devlin, K. P.; Grebenkemper, J. H.; Lee, K.; Cerretti, G.; Bux, S. K.; Kauzlarich, S. M. Enhancement of the Thermal Stability and Thermoelectric Properties of Yb₁₄MnSb₁₁ by Ce Substitution. Chem. Mater. 2020, 32, 9268-9276.
- (34) Vasilyeva, I.; Abdusalyamova, M.; Makhmudov, F.; Eshov, B.; Kauzlarich, S. Thermal Air-Oxidized Coating on Yb14-xRExMnSb11 Ceramics. J. Therm. Anal. Calorim. 2019, 136, 541-548.
- (35) Paik, J. A.; Brandon, E.; Caillat, T.; Ewell, R.; Fleurial, J. P. Life Testing of Yb14MnSb11 for High Performance Thermoelectric Couples. Nucl. Emerg. Technol. Sp. 2011, NETS-2011 2011, 616-622.
- (36) Petříček, V.; Dušek, M.; Palatinus, L. Crystallographic Computing System JANA2006: General Features. Z. Kristallogr. -Cryst. Mater. 2014, 229, 345-352.
- (37) Ong, S. P.; Richards, W. D.; Jain, A.; Hautier, G.; Kocher, M.; Cholia, S.; Gunter, D.; Chevrier, V. L.; Persson, K. A.; Ceder, G. Python Materials Genomics (Pymatgen): A Robust, Open-Source Python Library for Materials Analysis. Comput. Mater. Sci. 2013, 68, 314-319.
- (38) Okamoto, H. Sb-Yb (Antimony-Ytterbium). J. Phase Equilib. Diffus. 2008, 29, 473.